Goal-Oriented Discretization Error Control in Coupled Nearfield-Farfield Low-Boom Simulations

Marian Nemec* and Michael J. Aftosmis†
NASA Ames Research Center, Moffett Field, CA 94035, USA

Sriram K. Rallabhandi‡
NASA Langley Research Center, Hampton, VA 23681, USA

David L. Rodriguez§
Science & Technology Corp., Moffett Field, CA 94035, USA

The method of adjoint weighted residuals is used to determine the level of discretization error in loudness predictions of sonic booms on the ground. We analyze the standard nearfied-farfield domain decomposition approach. In the nearfield domain, the three-dimensional Euler equations are solved to obtain a pressure signature generated by the aircraft. In the farfield, this waveform is propagated through the atmosphere to the ground by solving the augmented Burgers' equation. Loudness is characterized using weighted sound-exposure-level metrics. We formulate discretization error estimates for the ground signature and loudness metrics for this one-way coupled system. Although the nearfield solution is independent of the farfield, the adjoint formulation for the coupled system provides feedback from the farfield to identify high-error regions in the nearfield. The results demonstrate that the discrete adjoint implementation is asymptotically consistent and provides reliable error estimates. Furthermore, we show how the error can be controlled through adaptive refinement of the nearfield mesh. The approach is evaluated on two- and three-dimensional problems, including the X-59 flight demonstration aircraft.

I. Introduction

The key to credible low-boom simulations is the control of discretization errors. While discretization errors plague essentially all numerical simulations, several factors conspire to make the prediction of sonic-booms especially sensitive. Perhaps the most obvious is the large domain with many disparate scales — the output of interest is loudness on the ground generated from a cruising altitude of around 50,000 ft by an aircraft roughly 100 ft long.[1] Moreover, the flow is shock-dominated, and includes the aircraft's boundary layer and engine plumes, shock-plume interactions, and shock propagation through a stratified and windy atmosphere.[2]

To efficiently handle the scale disparity, most sonic-boom simulations find ways to exploit the hyperbolic nature of these problems once sufficiently far away from the aircraft. Currently, the standard approach is to split the domain into the nearfield and farfield subdomains, as illustrated in Fig. 1. A steady, three-dimensional Euler or RANS simulation is used in the nearfield to determine the nearfield pressure signature (waveform). We emphasize that Fig. 1 is not drawn to scale — the signature is usually extracted within several hundred meters of the aircraft, while the cruising altitude can be in the upper troposphere. The nearfield signature initializes an atmospheric propagation in the farfield. This domain decomposition was introduced by Page and Plotkin,[3] has been thoroughly validated[4–8] and is being used extensively in the design of the new X-59 low-boom aircraft. Promising alternatives that seek to generalize this approach and

*Aerospace Engineer, Computational Aerosciences Branch, MS 258-5; marian.nemec@nasa.gov, Senior Member AIAA.
†Aerospace Engineer, Computational Aerosciences Branch; michael.aftosmis@nasa.gov, Associate Fellow AIAA.
‡Aerospace Engineer, Aeronautics Systems Analysis Branch; sriram.rallabhandi@nasa.gov, Associate Fellow AIAA.
§Senior Research Scientist, Computational Aerosciences Branch; david.l.rodriguez@nasa.gov, Senior Member AIAA.

reduce computational cost involve the use of midfield solvers[9,10] and fullfield approaches where segmentation of the domain is used.[11,12]

Excessive dissipation of shocks is especially challenging in the nearfield due to the three-dimensional nature of the flow. The attenuation effects worsen as the design loudness decreases and are a major concern at the current design target of 75 dB for the X-59. To address this, specialized topologies and techniques have been developed that facilitate manual construction of nearfield grids to minimize signal loss.[4,13,14] Moreover, there has been significant progress in automatic mesh adaptation for determining nearfield pressure signatures.[15] In particular, robust mesh convergence of nearfield signatures has been demonstrated using the method of adjoint-weighted residuals,[16–19] resulting in satisfactory convergence of ground loudness predictions.[20,21] A potential shortcoming in these simulations, however, is that the chosen norm of the nearfield pressure signature driving the mesh refinement acts only as a noise surrogate, since there is no feedback from the farfield subdomain. This means that the resulting nearfield mesh may not be "optimal" for farfield functionals and there is no easy way to leverage the nearfield error estimate to formally bound farfield outputs.

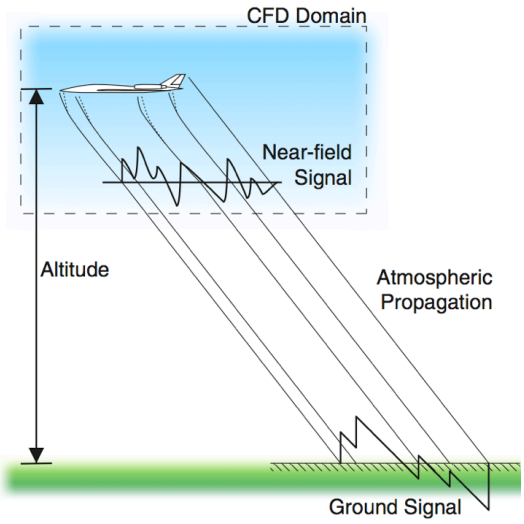


Figure 1: Sonic-boom domain decomposition

To address these issues, the present work extends the method of adjoint-weighted residuals[19,22–26] to enable direct error estimation for ground pressure signatures and loudness metrics computed via the nearfield-farfield domain decomposition. Since the farfield propagation is a lower-dimensional problem, we focus on automatic adaptation of the nearfield mesh that maximizes the accuracy of farfield outputs. The idea is to use the solution of adjoint equations derived for farfield outputs to weight the nearfield residuals. In other words, we use adjoints to provide feedback from the farfield to determine which features of the nearfield solution matter. Our work is motivated by the ideas of Rallabhandi and Park,[27] who explored the use of adjoint-based error estimates for boom-loudness predictions.

Goal-oriented error estimation has been previously extended from fluid flow problems to various multi-disciplinary applications. Examples include heat transfer,[28] fluid-structure interactions[29] and multi-species flow.[30] Carey *et al.*[31] present error representation formulas for general one-way coupled systems similar to the nearfield-farfield decomposition considered here. Their analysis assumes a finite-element discretization and compares adjoint formulations for coupled systems with various operator and domain splittings. In this work, we use a similar approach and consider a finite volume discretization of a steady problem in the nearfield[17,19,20] coupled with a finite-difference discretization of an unsteady problem in the farfield.[32,33] The outputs of interest are various weightings of the Sound Exposure Level metric (A/B/C/D-SEL [dB]) used to characterize sonic-boom loudness. We construct a reliable error estimate for these outputs and we use it to guide adaptive mesh refinement. Several two- and three-dimensional test cases are presented to verify the accuracy of this error estimate and to benchmark the computational efficiency of this approach.

II. Problem Formulation and Governing Equations

To compute sonic-boom loudness, the problem domain is divided into slightly overlapping nearfield Ω_N and farfield Ω_F regions, as illustrated in Fig. 1. In the nearfield, we solve the steady, three-dimensional Euler equations governing compressible flow of a perfect gas to determine the nearfield pressure signature. For a finite region of space with volume V and surface area A, the integral form of the Euler equations is given by

$$\frac{\mathrm{d}}{\mathrm{d}t}\int_V \vec{\mathbf{Q}}\,\mathrm{d}V + \oint_A \bar{\mathbf{F}}\cdot\hat{\mathbf{n}}\,\mathrm{d}A = \mathbf{0} \tag{1}$$

where $\vec{\mathbf{Q}} = [\rho, \rho\vec{\mathbf{U}}, \rho E]^{\mathrm{T}} = [\rho, \rho u, \rho v, \rho w, \rho E]^{\mathrm{T}}$ are the non-dimensional conserved variables, and

$$\bar{\mathbf{F}} \cdot \hat{\mathbf{n}} = \begin{bmatrix} \rho U_{\mathrm{n}} \\ \rho U_{\mathrm{n}} \vec{\mathbf{U}} + p\hat{\mathbf{n}} \\ (\rho E + p) U_{\mathrm{n}} \end{bmatrix} \tag{2}$$

where $U_{\mathrm{n}} = \vec{\mathbf{U}} \cdot \hat{\mathbf{n}}$ and $\hat{\mathbf{n}}$ is the outward facing unit normal. In the farfield, the evolution of the nearfield waveform as it descends through a stratified and windy atmosphere to the ground is modeled using geometric acoustics in conjunction with the augmented Burgers' equation[32,34,35] in non-dimensional form

$$\frac{\partial P}{\partial \sigma} = \frac{\partial P^2}{\partial \tau} + \frac{1}{\Gamma}\frac{\partial^2 P}{\partial \tau^2} + \sum_{\nu} C_\nu \left(1 + \theta_\nu \frac{\partial}{\partial \tau}\right)^{-1} \frac{\partial^2 P}{\partial \tau^2} - \frac{P}{2S}\frac{\partial S}{\partial \sigma} + \frac{P}{\rho_0 c_0}\frac{\partial(\rho_0 c_0)}{\partial \sigma} \tag{3}$$

where $P = \frac{p_0}{p_{\mathrm{r}}} p'$ is a pressure perturbation p' scaled by the ratio of local ambient and reference pressures, σ the distance along a ray path, τ the retarded time, C_ν the dispersion parameter, Γ the thermoviscous parameter, θ_ν the molecular-relaxation time parameter of the ν^{th} relaxation process, ρ_0 and c_0 the local density and speed of sound, respectively, and S the ray tube area of adjacent ray paths.

Equations 1 and 3 are coupled at a boundary condition located a few body lengths away from the aircraft

$$P(\sigma = A_{\mathrm{c}} - L_\perp, \tau) = p'(\mathbf{x}) \quad \mathbf{x} \in \ell \in \Omega_{\mathrm{N}} \tag{4}$$

where A_{c} is the cruise altitude, $L_\perp$ is the normal distance between the aircraft centerline and the location of the line sensor ℓ that is used to extract the pressure signature $p' = (p - p_\infty)/p_\infty$ from Ω_{N}. Note that $L_\perp \ll A_{\mathrm{c}}$ and that the steady pressure signature along ℓ intializes the propagation in the time domain, i.e., along τ, based on the cruise Mach number M_∞ of the aircraft.

The primary output quantities of interest are the ground pressure signature and the loudness metrics derived from the ground signature, namely the various weightings of the sound exposure levels (A/B/C/D-SEL [dB]). These are not only evaluated directly under the flight path (on-track), as indicated in Fig. 1, but also off-track to determine the full sonic-boom carpet.[2]

III. Discretization Error Analysis

A. Review of Single-Discipline Systems

We begin with a summary of the method of adjoint-weighted residuals for finite-volume and finite-difference discretizations based on Refs. 19, 23, 25. Consider a tessellation $\mathcal{T}_{\mathrm{H}}$ with characteristic cell size H of domain Ω. Compute a discrete solution $\mathbf{Q}(\mathbf{x})$ that satisfies the simulation

$$\mathbf{R}(\mathbf{Q}) = 0 \qquad \mathbf{x} \in \mathcal{T}_{\mathrm{H}} \tag{5}$$

where $\mathbf{R}$ is a residual operator that includes all boundary conditions. For example, $\mathbf{R}$ and $\mathbf{Q}$ could represent the nearfield or farfield residual operator and solution, respectively, for the problem introduced in Sec. II. Let $J(\mathbf{Q})$ be a user-selected scalar output of the simulation, such as drag in the nearfield or sonic-boom loudness in the farfield. The classic approach for estimating the level of discretization error ε in $J(\mathbf{Q})$ involves uniformly refining $\mathcal{T}_{\mathrm{H}}$ to obtain $\mathcal{T}_{\mathrm{h}}$, solving for $J(\mathbf{Q}_{\mathrm{h}})$, computing the error relative to the embedded mesh

$$e = |J(\mathbf{Q}_{\mathrm{h}}) - J(\mathbf{Q})| \tag{6}$$

and then relying on asymptotic analysis[36] to determine the total discretization error

$$\varepsilon = \left(1 + \frac{1}{r^p - 1}\right) e \tag{7}$$

where p is the order of accuracy of the spatial discretization and r is the refinement ratio, H/h.

In practice, the first challenge in using Eq. 6 is to obtain a reliable estimate for $J(\mathbf{Q}_{\mathrm{h}})$ without solving on $\mathcal{T}_{\mathrm{h}}$ to avoid the prohibitive computational cost. The second challenge is to not only determine ε, but also to estimate the distribution of ε in $\mathcal{T}_{\mathrm{H}}$, so that we can adaptively refine $\mathcal{T}_{\mathrm{H}}$ to minimize the influence of

discretization error on J. To address both challenges, let $\mathbf{q} = \mathbf{M}\mathbf{Q}$, where $\mathbf{M}$ is a prolongation matrix that reconstructs the solution from $\mathcal{T}_\mathrm{H}$ to $\mathcal{T}_\mathrm{h}$, and linearize $J(\mathbf{Q}_\mathrm{h})$ to obtain

$$J(\mathbf{Q}_\mathrm{h}) \approx J(\mathbf{q}) + \frac{\partial J(\mathbf{q})}{\partial \mathbf{Q}_\mathrm{h}}(\mathbf{Q}_\mathrm{h} - \mathbf{q}) \tag{8}$$

To eliminate the dependence on $\mathbf{Q}_\mathrm{h}$, linearize the embedded-mesh residual

$$\mathbf{R}(\mathbf{Q}_\mathrm{h}) = \mathbf{0} \approx \mathbf{R}(\mathbf{q}) + \frac{\partial \mathbf{R}(\mathbf{q})}{\partial \mathbf{Q}_\mathrm{h}}(\mathbf{Q}_\mathrm{h} - \mathbf{q}) \tag{9}$$

and obtain

$$J(\mathbf{Q}_\mathrm{h}) \approx J(\mathbf{q}) - \Psi_\mathrm{h}^\mathrm{T}\mathbf{R}(\mathbf{q}) \tag{10}$$

where

$$\left[\frac{\partial \mathbf{R}(\mathbf{q})}{\partial \mathbf{Q}_\mathrm{h}}\right]^\mathrm{T} \Psi_\mathrm{h} = \frac{\partial J(\mathbf{q})}{\partial \mathbf{Q}_\mathrm{h}}^\mathrm{T} \tag{11}$$

Equation 11 is an adjoint equation. It is a system of linear equations independent of $\mathbf{Q}_\mathrm{h}$, but impractical to solve because $\mathcal{T}_\mathrm{h}$ is large. To circumvent this difficulty, we rewrite Eq. 10 using an adjoint solution obtained from $\mathcal{T}_\mathrm{H}$

$$J(\mathbf{Q}_\mathrm{h}) \approx J(\mathbf{q}) - \boldsymbol{\psi}^\mathrm{T}\mathbf{R}(\mathbf{q}) - (\Psi_\mathrm{h} - \boldsymbol{\psi})^\mathrm{T}\mathbf{R}(\mathbf{q}) \tag{12}$$

where $\boldsymbol{\psi} = \mathbf{M}\Psi$ is a prolongation of the adjoint solution from the working mesh to the embedded mesh. The adjoint variables Ψ satisfy

$$\left[\frac{\partial \mathbf{R}(\mathbf{Q})}{\partial \mathbf{Q}}\right]^\mathrm{T} \Psi = \frac{\partial J(\mathbf{Q})}{\partial \mathbf{Q}}^\mathrm{T} \qquad \mathbf{x} \in \mathcal{T}_\mathrm{H} \tag{13}$$

We split Eq. 12 into an expression for the corrected functional

$$J_c = J(\mathbf{q}) - \boldsymbol{\psi}^\mathrm{T}\mathbf{R}(\mathbf{q}) \tag{14}$$

and a higher-order remaining error term

$$\eta = (\tilde{\Psi}_\mathrm{h} - \boldsymbol{\psi})^\mathrm{T}\mathbf{R}(\mathbf{q}) \tag{15}$$

where $\tilde{\Psi}_\mathrm{h}$ is a higher-order reconstruction of Ψ used to approximate Ψ_h in Eq. 12. We use J_c to evaluate the error in Eq. 6 and use Eq. 15 to construct a cell-wise error indicator for mesh adaptation so that $|\eta| \to 0$ as $\mathrm{H} \to 0$. In each control volume of $\mathcal{T}_\mathrm{H}$, the error indicator is given by

$$\boldsymbol{\eta}_H = \sum_{j \in \mathcal{T}_\mathrm{h}} \left| \left(\tilde{\Psi}_\mathrm{h} - \boldsymbol{\psi}\right)^\mathrm{T} \mathbf{R}(\mathbf{q}) \right| \tag{16}$$

where j denotes the j^{th} child of each parent cell in $\mathcal{T}_\mathrm{H}$.

B. Extension to Multidisciplinary Triangular Systems

We now extend the discretization error analysis to one-way coupled systems. We specifically consider the two-discipline system described in Sec. II; however, the approach handles any number of disciplines. Consider a tessellation $\mathcal{T}_{\mathrm{N,H}}$ of the nearfield domain Ω_N and a tessellation $\mathcal{T}_{\mathrm{F,H}}$ of the farfield domain Ω_F. The two tessellations are independent. Let $\mathbf{Q}_\mathrm{N}$ and $\mathbf{R}_\mathrm{N}$ be the flow solution and the discrete residual operator of Eq. 1 in Ω_N, respectively, and $\mathbf{Q}_\mathrm{F}$ and $\mathbf{R}_\mathrm{F}$ be the pressure solution and the discrete residual operator of Eq. 3 in Ω_F, respectively. The coupled system can be written as

$$\mathbf{R}_\mathrm{N}(\mathbf{Q}_\mathrm{N}) = 0 \tag{17}$$

$$\mathbf{R}_\mathrm{F}(\mathbf{Q}_\mathrm{N}, \mathbf{Q}_\mathrm{F}) = 0 \tag{18}$$

where the residual operators include all boundary conditions. In particular, $\mathbf{R}_\mathrm{F}$ includes the residual of the transfer function defined by Eq. 4, as noted by its dependence on $\mathbf{Q}_\mathrm{N}$. We choose sonic-boom loudness on the ground, $J(\mathbf{Q}_\mathrm{F})$, as an output of interest of the coupled simulation. The coupled system is solved sequentially

since $\mathbf{Q}_\mathrm{N}$ is independent of $\mathbf{Q}_\mathrm{F}$. The level of discretization error in $J(\mathbf{Q}_\mathrm{F})$, however, depends on the accuracy of $\mathbf{Q}_\mathrm{N}$ via Eq. 18. Our goal is to construct an error representation formula for $J(\mathbf{Q}_\mathrm{F})$ that accounts for the discretization errors in $\mathbf{Q}_\mathrm{N}$, as well as $\mathbf{Q}_\mathrm{F}$.

To extend the method of adjoint-weighted residuals to one-way coupled systems, we redefine the solution vector and residual operators as

$$\mathbf{Q} = \begin{bmatrix} \mathbf{Q}_\mathrm{N} \\ \mathbf{Q}_\mathrm{F} \end{bmatrix} \quad \text{and} \quad \mathbf{R} = \begin{bmatrix} \mathbf{R}_\mathrm{N} \\ \mathbf{R}_\mathrm{F} \end{bmatrix} \tag{19}$$

Following the single-discipline analysis, the adjoint equation, Eq. 13, for the coupled system becomes

$$\begin{bmatrix} \frac{\partial \mathbf{R}_\mathrm{N}}{\partial \mathbf{Q}_\mathrm{N}} & \mathbf{0} \\ \frac{\partial \mathbf{R}_\mathrm{F}}{\partial \mathbf{Q}_\mathrm{N}} & \frac{\partial \mathbf{R}_\mathrm{F}}{\partial \mathbf{Q}_\mathrm{F}} \end{bmatrix}^\mathrm{T} \begin{bmatrix} \Psi_\mathrm{N} \\ \Psi_\mathrm{F} \end{bmatrix} = \begin{bmatrix} \frac{\partial \mathbf{R}_\mathrm{N}}{\partial \mathbf{Q}_\mathrm{N}}^\mathrm{T} & \frac{\partial \mathbf{R}_\mathrm{F}}{\partial \mathbf{Q}_\mathrm{N}}^\mathrm{T} \\ \mathbf{0} & \frac{\partial \mathbf{R}_\mathrm{F}}{\partial \mathbf{Q}_\mathrm{F}}^\mathrm{T} \end{bmatrix} \begin{bmatrix} \Psi_\mathrm{N} \\ \Psi_\mathrm{F} \end{bmatrix} = \begin{bmatrix} \mathbf{0} \\ \frac{\partial J}{\partial \mathbf{Q}_\mathrm{F}}^\mathrm{T} \end{bmatrix} \tag{20}$$

where we use the short form $\partial \mathbf{R}/\partial \mathbf{Q}$ for $\partial \mathbf{R}(\mathbf{Q})/\partial \mathbf{Q}$. We observe that the system Jacobian matrix is block lower triangular and its transpose is upper triangular. This matrix structure decouples the farfield adjoint variables from the nearfield, which allows a sequential solution procedure. The single-discipline farfield adjoint equation is solved first

$$\left[\frac{\partial \mathbf{R}_\mathrm{F}(\mathbf{Q}_\mathrm{F})}{\partial \mathbf{Q}_\mathrm{F}}\right]^\mathrm{T} \Psi_\mathrm{F} = \frac{\partial J(\mathbf{Q}_\mathrm{F})}{\partial \mathbf{Q}_\mathrm{F}}^\mathrm{T} \tag{21}$$

followed by an adjoint for the nearfield with a modified right hand side

$$\left[\frac{\partial \mathbf{R}_\mathrm{N}(\mathbf{Q}_\mathrm{N})}{\partial \mathbf{Q}_\mathrm{N}}\right]^\mathrm{T} \Psi_\mathrm{N} = -\left[\frac{\partial \mathbf{R}_\mathrm{F}(\mathbf{Q}_\mathrm{N}, \mathbf{Q}_\mathrm{F})}{\partial \mathbf{Q}_\mathrm{N}}\right]^\mathrm{T} \Psi_\mathrm{F} \tag{22}$$

Equation 22 is critical because it quantifies how perturbations in the nearfield governing equations affect the output in the farfield.

To form expressions for the corrected functional and error terms analogous to Eqs. 14 and 15, let

$$\mathbf{q}_\mathrm{N} = \mathbf{M}_\mathrm{N} \mathbf{Q}_\mathrm{N} \tag{23}$$

$$\mathbf{q}_\mathrm{F} = \mathbf{M}_\mathrm{F} \mathbf{Q}_\mathrm{F} \tag{24}$$

where $\mathbf{M}_\mathrm{N}$ and $\mathbf{M}_\mathrm{F}$ are prolongation operators that reconstruct the solutions in $\mathcal{T}_{\mathrm{N,h}}$ and $\mathcal{T}_{\mathrm{F,h}}$, respectively. Note that $\mathbf{M}_\mathrm{F}$ involves reconstruction in space-time. Similarly, define $\boldsymbol{\psi}_\mathrm{N} = \mathbf{M}_\mathrm{N} \Psi_\mathrm{N}$ and $\boldsymbol{\psi}_\mathrm{F} = \mathbf{M}_\mathrm{F} \Psi_\mathrm{F}$ for the reconstructed adjoint solutions in $\mathcal{T}_{\mathrm{N,h}}$ and $\mathcal{T}_{\mathrm{F,h}}$, respectively. The corrected functional for the coupled system becomes

$$J_c = J(\mathbf{q}_\mathrm{F}) - \begin{bmatrix} \boldsymbol{\psi}_\mathrm{N}^\mathrm{T} & \boldsymbol{\psi}_\mathrm{F}^\mathrm{T} \end{bmatrix} \begin{bmatrix} \mathbf{R}_\mathrm{N}(\mathbf{q}_\mathrm{N}) \\ \mathbf{R}_\mathrm{F}(\mathbf{q}_\mathrm{N}, \mathbf{q}_\mathrm{F}) \end{bmatrix} \tag{25}$$

and the remaining error terms are given by

$$\eta_\mathrm{N} = (\tilde{\Psi}_{\mathrm{N,h}} - \boldsymbol{\psi}_\mathrm{N})^\mathrm{T} \mathbf{R}_\mathrm{N}(\mathbf{q}_\mathrm{N}) \tag{26}$$

$$\eta_\mathrm{F} = (\tilde{\Psi}_{\mathrm{F,h}} - \boldsymbol{\psi}_\mathrm{F})^\mathrm{T} \mathbf{R}_\mathrm{F}(\mathbf{q}_\mathrm{N}, \mathbf{q}_\mathrm{F}) \tag{27}$$

where $\tilde{\Psi}_{\mathrm{N,h}}$ and $\tilde{\Psi}_{\mathrm{F,h}}$ are higher order approximations of the adjoint solutions from $\mathcal{T}_{\mathrm{N,H}}$ and $\mathcal{T}_{\mathrm{F,H}}$. The mesh refinement indicators η_N and η_F are a straightforward extension of Eq. 16 to each subdomain.

We note a special case that we exploit in this work. Since the propagation problem involves fewer unknowns and is lower-dimensional, the computational cost of obtaining the nearfield solution is significantly higher than that of the farfield. This means that the time penalty for propagation is relatively small. In addition, the error distribution in $\mathcal{T}_{\mathrm{F,H}}$ is not required because our propagation code is currently limited to a uniform discretization. We take advantage of these circumstances and solve an additional propagation problem in the embedded farfield domain $\mathcal{T}_{\mathrm{F,h}}$

$$\mathbf{R}_\mathrm{F}(\mathbf{q}_\mathrm{N}, \mathbf{Q}_{\mathrm{F,h}}) = 0 \tag{28}$$

to directly compute $\mathbf{Q}_{\mathrm{F,h}}$. This simplifies Eq. 25 for the corrected functional

$$J_c^\star = J(\mathbf{Q}_{\mathrm{F,h}}) - \boldsymbol{\psi}_{\mathrm{N}}^{\mathrm{T}} \mathbf{R}_{\mathrm{N}}(\mathbf{q}_{\mathrm{N}}) \tag{29}$$

since the farfield residual is satisfied exactly on $\mathcal{T}_{\mathrm{F,h}}$. This means that for a user-selected set of farfield outputs we require one solution of Eq. 17 and 18 on $\mathcal{T}_{\mathrm{N,H}}$ and $\mathcal{T}_{\mathrm{F,H}}$, respectively; a solution of the adjoint equations, Eqs. 21-22, for each output on $\mathcal{T}_{\mathrm{N,H}}$ and $\mathcal{T}_{\mathrm{F,H}}$; and one solution of Eq. 18 on the embedded mesh, $\mathcal{T}_{\mathrm{F,h}}$.

IV. Implementation

In the nearfield, Eq. 1 is discretized on a multilevel Cartesian mesh with embedded boundaries. $\mathcal{T}_{\mathrm{N,H}}$ consists of regular Cartesian hexahedra everywhere, except for a layer of body-intersecting cells, or cut cells, adjacent to the wetted surface of the geometry, as illustrated in Fig. 2. The $\mathbf{R}_{\mathrm{N}}$ operator in Eq. 17 represents a cell-centered, second-order accurate finite volume method based on the flux-vector splitting approach of van Leer.[37] Steady-state flow solutions are obtained using an explicit, five-stage scheme with local time-stepping, multigrid, and a domain decomposition scheme for parallel computing.[38–40] All boundary conditions are enforced weakly.[41,42] The prolongation matrix $\mathbf{M}_{\mathrm{N}}$ in Eq. 23 is tri-linear reconstruction and $\tilde{\Psi}_{\mathrm{N,h}}$ in Eq. 26 is constructed using limited tri-quadratic interpolation. Ref. 19 provides details on the formulation and solution of the adjoint equation, computation of discretization error estimates and mesh adaptation in the nearfield domain. The implementation used in this work is Cart3D version 1.5.7.[43]

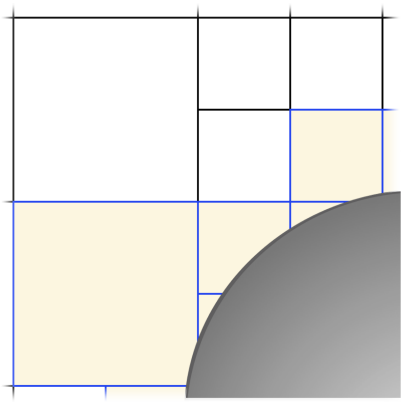


Figure 2: Multilevel Cartesian mesh with a cut-cell boundary (highlighted)

In the farfield, Eq. 3 is discretized on a uniform mesh in τ and is solved along ray paths that account for the state of the atmosphere in σ.[32,34] An operator splitting approach is used to separate the terms on the right side of Eq. 3 into five equations that handle the effects of nonlinearity, thermoviscous absorption, molecular relaxation, ray-tube spreading and atmospheric stratification. The implementation used in this work is sBOOM version 2.86.[44] Significant modifications, however, are required to obtain an adjoint consistent discretization. The original approach to handle the nonlinearity (first term on right side of Eq. 3) used a non-conservative form and a Poisson solution procedure. This is replaced by a conservative finite-volume discretization. In Eq. 18, the $\mathbf{R}_{\mathrm{F}}$ operator for the nonlinearity represents Godunov's flux function with explicit Euler time marching, and $\mathbf{Q}_{\mathrm{F}} \equiv \mathbf{P}$. A minor modification is also made in the linearization of the absorption equation (second term on right side of Eq. 3). In the primal solver, the local absorption coefficient is artificially increased when excessive shock jumps are detected.[34] This limiting procedure is treated as a constant in the linearization. Finally, adjoint consistent discretization has not yet been implemented for the relaxation term (third term on right side of Eq. 3). Consequently, in some test cases in Sec.V we neglect relaxation to carefully study error propagation in the coupled system, while in others relaxation is included in the primal solve but then treated as a constant in the linearization.

While the adjoint equation, Eq. 21, represents a large space-time system, the solution procedure is relatively straightforward and involves marching the system of equations from the farfield to the nearfield.[33] The nearfield and farfield solvers have been thoroughly validated for use in sonic-boom prediction.[7,17,20,21] The discretized form of the transfer function, Eq. 4, from the adapted (non-uniform) nearfield to the farfield is given by

$$\mathbf{P}_\tau^0 = \mathbf{L}\mathbf{p}' \tag{30}$$

where $\mathbf{P}_\tau^0 = [P_1^0, P_2^0, \ldots, P_{M_\tau}^0]^{\mathrm{T}}$ is the pressure perturbation for the M_τ uniformly spaced nodes in τ used to initialize the propagation when $\sigma = 0$, $\mathbf{L}$ is generally a rectangular matrix holding linear interpolation weights, and $\mathbf{p}'$ represents the pressure perturbations from the nearfield solver along the line sensor. When the output of interest is the ground pressure signature, the discrete functional form is given by

$$J_{\mathrm{G}} = \frac{1}{M_\tau} \sum_{i=0}^{M_\tau} P_i^2 \tag{31}$$

and we use the notation J_{A}, J_{B}, J_{C} and J_{D} to represent A/B/C/D-SEL outputs, respectively.

V. Results

All test cases assume a standard atmosphere with no wind. In addition, CFL = 1/2 is used to propagate all signatures from the nearfield to the ground.

A. Farfield Adjoint Convergence Study: N-Wave Propagation

Due to the changes in the farfield solver as described in Sec. IV, we begin with a canonical problem to verify the solution of the farfield primal and adjoint equations. We consider the propagation of an N-wave using conditions from Case 2 of the Third AIAA Sonic Boom Propagation Workshop.[7,45] The propagation is from an altitude of 16,459.2 m to a ground height of 110.011 m and the Mach number is 1.4. We use a nearfield sensor of length 100 m to initialize the propagation

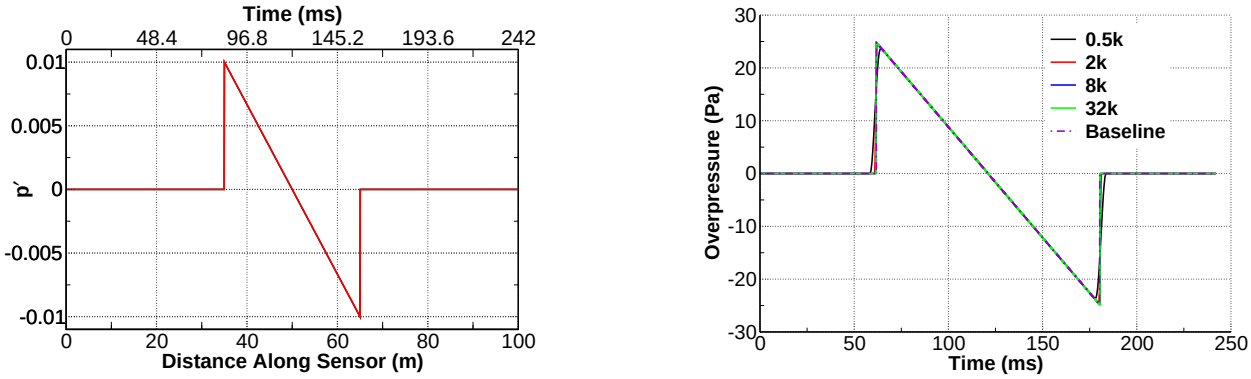
$$\mathbf{p}' = -0.01 \times \begin{cases} \frac{(x_i - 50)}{15} & \text{if } 35 \leq x_i \leq 65 \\ 0 & \text{otherwise} \end{cases} \tag{32}$$

Figure 3a shows the nearfield signature along the sensor and in the time domain corresponding to the flight Mach number and cruise altitude.

We consider a sequence of nested refinements of the sensor, doubling from 501 to 32,001 nodes. The discretization along the sensor matches $\mathbf{P}^0_\tau$ in Eq. 30. This reduces $\mathbf{L}$ in Eq. 30 to an identity matrix. The corresponding discretization along the ray path to the ground is done at constant CFL, i.e., $\Delta\sigma = \text{CFL}\ \Delta\tau / \max(|\mathbf{P}^n|)$. Figure 3b shows ground signatures from selected refinement levels. As expected, the increasing resolution improves the sharpness of the discontinuities. There is minimal rounding of the shock jumps because relaxation has been omitted due to the incomplete linearization of this term in the adjoint. The waveform labeled Baseline in Fig. 3b is obtained with the original solver, i.e., without our modification of handling the nonlinearity term, on the finest mesh. We observe excellent agreement between the solvers. Moreover, the solvers agree to within 0.05% in all SEL outputs. Comparing Fig. 3b with Fig. 3a, we observe that the period increases from approximately 75 ms to 120 ms.

Figure 4 shows the attenuation and spreading of the N-wave in terms of $\mathbf{P}$ and retarded time τ, when $\sigma = 0$ (Nearfield) and $\sigma = \sigma_G$ (Ground). Figure 4 also shows the solution of the adjoint equation, Eq. 21, for the ground signature output, Eq. 31. Recall that the adjoint solution is initialized in the farfield and marches backward to the nearfield. Hence, the width of the adjoint solution is fixed by the period of the ground signature, as shown in Fig. 4. Furthermore, we observe that the adjoint variable is continuous across the shocks of the N-wave throughout the propagation. This agrees with the analytic adjoint of Burgers' equation.[46,47]

Figure 5 shows adjoint solutions for the ground signature, Eq. 31, and C-SEL outputs for selected refinement levels. Since $\mathbf{L}$ in Eq. 30 is an identity matrix, the matrix $\partial\mathbf{R}_F/\partial\mathbf{Q}_N$ in Eq. 22 is also an identity matrix, which means $\Psi_F \equiv \partial J/\partial p'$. The adjoint solution is converging for both outputs and there are no spurious oscillations. This indicates that the discretization is adjoint consistent. Similar results are obtained



(a) Nearfield Signature

(b) Ground Signature

Figure 3: Intial N-wave (left) and convergence of ground signature with uniform refinement (right).

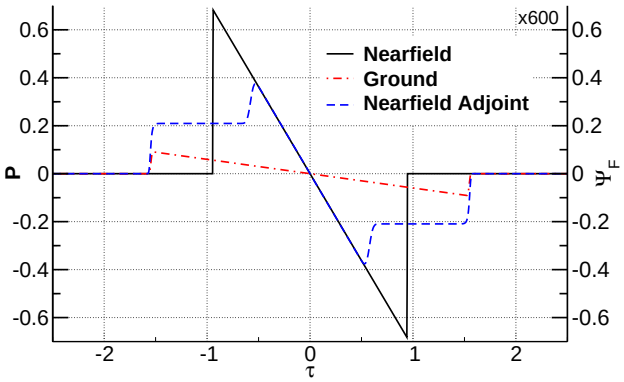
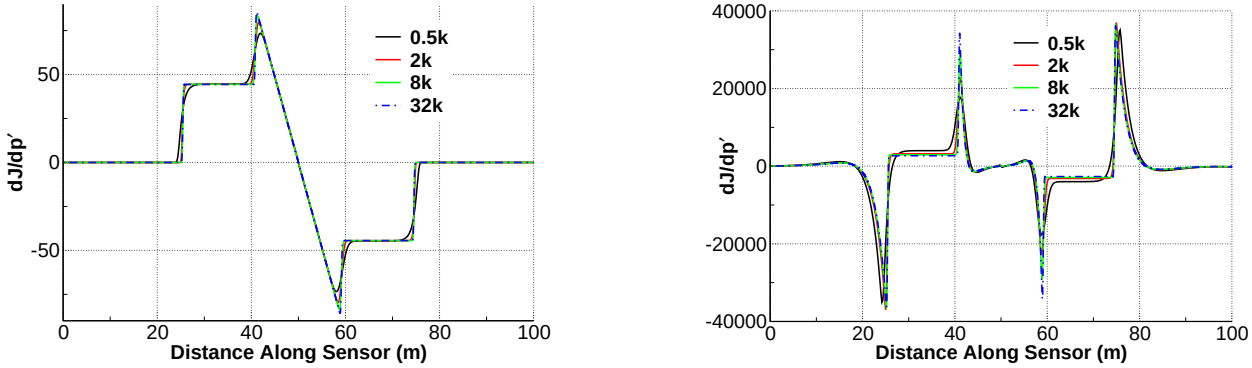


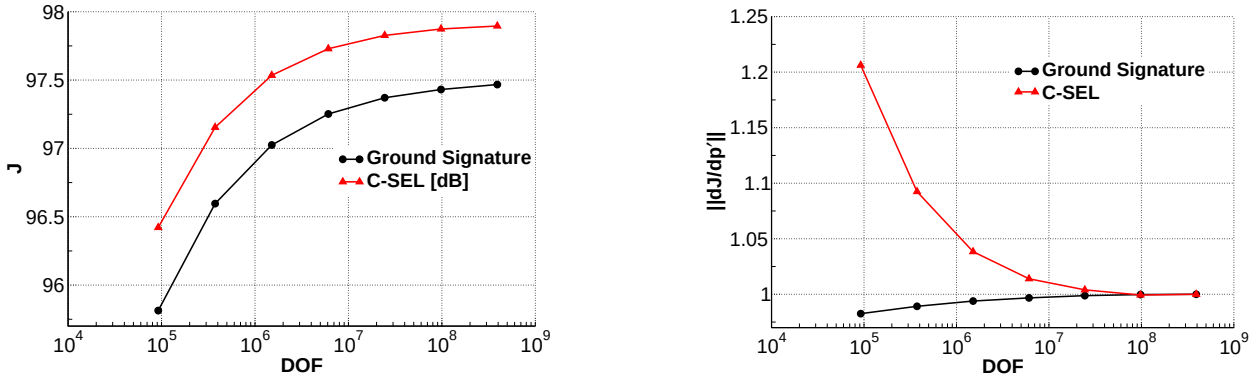
Figure 4: Nearfield and ground N-waves, and the nearfield adjoint for the ground-signature output. The adjoint solution is scaled by a factor of 600 to allow comparison with features of the waveforms.



(a) Ground Signature

(b) C-SEL

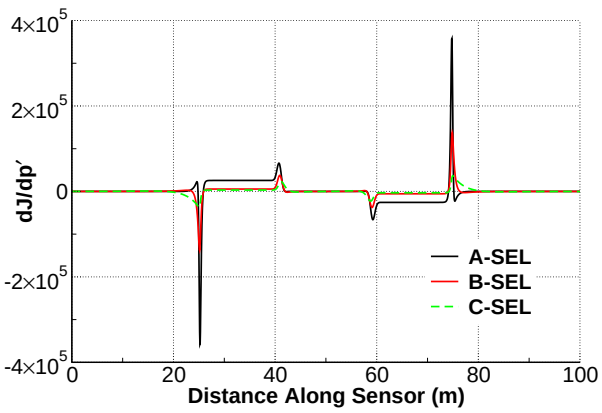
Figure 5: Convergence of Ψ_F (also $\partial J/\partial p'$) along the nearfield sensor with uniform refinement from 501 to 32,001 nodes and constant CFL.



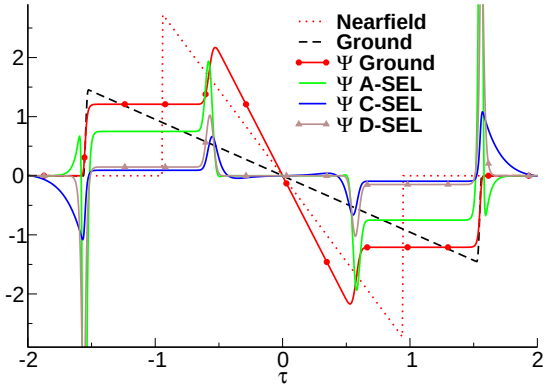
(a) Ground signature (scaled by 2,200) and C-SEL

(b) Gradients

Figure 6: Convergence of output functionals (left) and normalized gradient norms (right) with uniform refinement from 501 to 32,001 nodes and constant CFL.



(a) Farfield gradients for A/B/C-SEL outputs



(b) Close-up view of N-waves and adjoint solutions as a function of retarded time τ

Figure 7: Characteristics of gradients and adjoint solutions, Ψ, for the ground signature and selected metrics.

for the A/B/D-SEL outputs. Figure 6 provides further evidence of convergence for the output functionals and gradient norms. The values are plotted against the degrees of freedom (DOF) of each simulation. This is a product of the M_τ points used to discretize the signature and the M_σ steps taken to propagate the signature to the ground. Figure 6a shows first-order convergence of the outputs, which is consistent with the discretization. Similarly, Fig. 6b shows first-order convergence of normalized gradient norms.

The differences in character of the adjoint solutions shown in Fig. 5 is striking. The solutions reveal how perturbations along the nearfield signature affect the output functional. The adjoint for the ground signature output in Fig. 5a correlates with the movement of the front and aft shocks as the N-wave descends. In contrast, Fig. 5b shows that C-SEL is most sensitive to the start and end locations of the ground signature. We examine these features more closely in Fig. 7a, which shows that the adjoint solutions for the A- and B-SEL outputs are similar to C-SEL, but more sensitive. D-SEL is not shown because it is very similar to B-SEL at this scale. Note that the spikes in the A-SEL adjoints are roughly a factor of ten larger than those for C-SEL. Figure 7b provides a close-up view of the adjoint variables, Ψ, to highlight the alignment of the features of the adjoint solution with those of the N-wave. In this plot, the nearfield signature and SEL metric adjoints have been scaled by a factor of 4, the ground signature by 32 and the adjoint corresponding to the ground signature by 4,096. We observe that all the SEL adjoints show high sensitivity in regions where the ground-signature adjoint is discontinuous and are close to zero through the expansion region of the nearfield N-wave. Furthermore, observe the non-zero values of the SEL adjoints upstream and downstream of the ground N-wave due to the sensitivity of these metrics to different frequencies. We investigate the changes in the zone of dependence in the nearfield domain that are a direct consequence of these farfield solutions in the next test case.

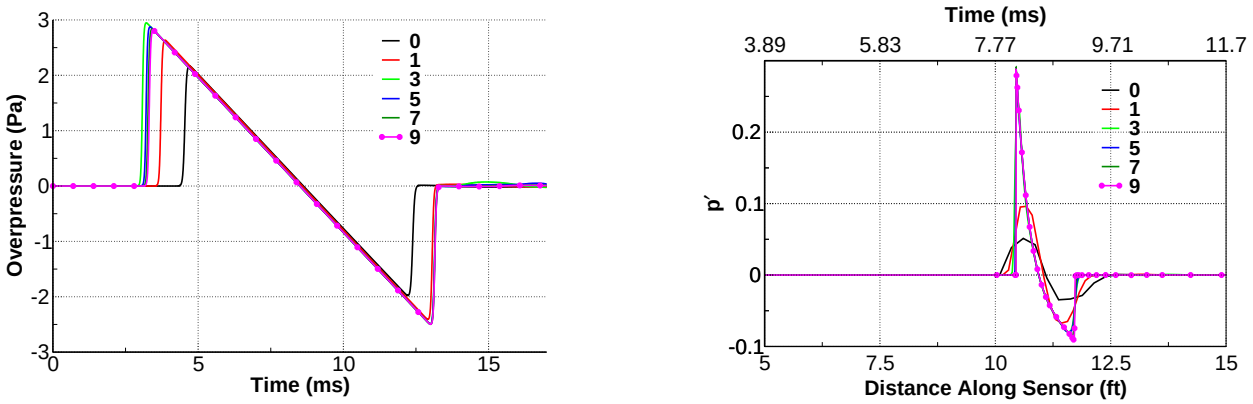
B. Nearfield-Farfield Model Problem: NACA 0003 Airfoil

This case considers a model problem for the nearfield-farfield coupled system. We consider a flow simulation for the thin NACA 0003 airfoil with a 1 ft chord at $M_\infty = 1.3$, $\alpha = 0°$, and altitude of 54,000 ft. The line sensor location for the nearfield-farfield interface, Eq. 4, is set at half-a-chord below the airfoil[a]. We specify a sensor length of 22 chords, extending 8 chords in front of the airfoil. The nearfield domain boundary is 64 chords away.

For goals of the simulation, we choose to predict the ground signature, J_G, and the D-SEL metric[b], J_D. In the nearfield domain, we start the simulation on a coarse initial mesh with cell-size $H = 0.25$ chords. Once a steady-state solution of Eq. 17 is reached, the nearfield signature is transferred to the farfield domain via Eq. 30 and Eq. 18 is solved to propagate the signature to the ground to evaluate the outputs. The propagation is performed on a fixed, uniform mesh $\mathcal{T}_{\mathrm{F,H}}$ of 10,000 nodes. We neglect molecular relaxation effects. To estimate the level of discretization error in the outputs, we solve the adjoint equations, first Eq. 21 followed by Eq. 22, for each output and compute the corrected functionals via Eq. 29. If the error level is too

[a]We choose a small extraction distance to reduce the problem size.

[b]Results for A/B-SEL are similar to D-SEL and we found the frequency response of C-SEL not appropriate for this problem.



(a) Ground signatures

(b) Nearfield signatures

Figure 8: Convergence of ground and nearfield signatures as a function of refinement in the nearfield domain for the ground signature output of the NACA 0003 test case. Every other adaptation cycle is plotted.

high, we use the error indicator given by Eq. 26 to adapt the nearfield mesh. The cell adaptation threshold is set a factor of two below the mean of the nearfield error distribution.

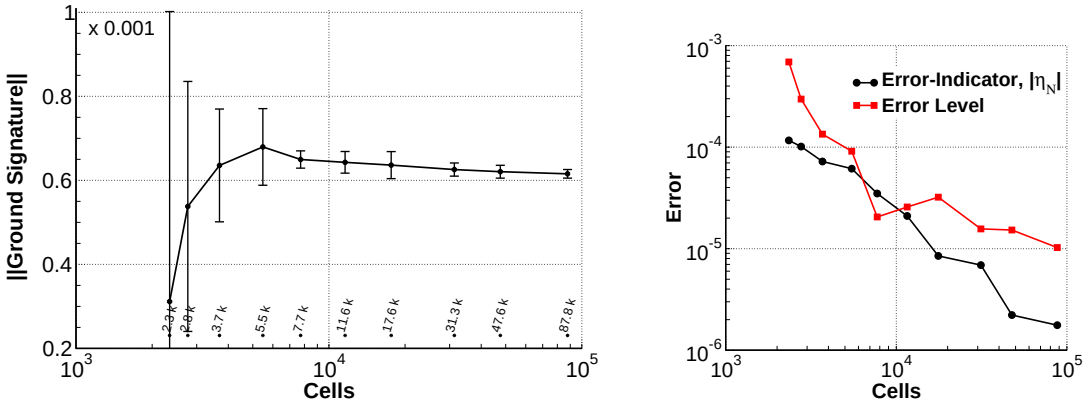
Figure 8a shows the evolution of the ground signature over nine refinement cycles for the ground signature output, Eq. 31. We obtain similar results for the D-SEL output. Figure 8b shows the corresponding nearfield signatures, plotted as a function of distance along the sensor in the nearfield domain and time in the farfield domain. Both the farfield and nearfield signatures converge to plotting accuracy in about 7 cycles. Note the ten-fold increase in the period of the signature from about 1 ms to over 10 ms. This is due to the strength of the shocks near the airfoil and the fact that the nearfield problem is constrained to two dimensions.

Figure 9 shows the convergence history of the farfield outputs as a function of the number of cells in the nearfield mesh. The error-indicator (black line in plots on right in Fig. 9) shows that the adaptation is systematically reducing the remaining-error term given by Eq. 26. The error levels ε (red lines) are obtained from Eq. 7 via Eq. 29 and these are decreasing as well. The size of the error bars in the plots on the left side of Fig. 9 corresponds to the error levels. Both outputs converge well, with error consistently decreasing once the nearfield mesh reaches about 20,000 cells. The simulations reach high accuracy on the finest mesh. For example, D-SEL converges to 72.5 ± 0.01 dB.

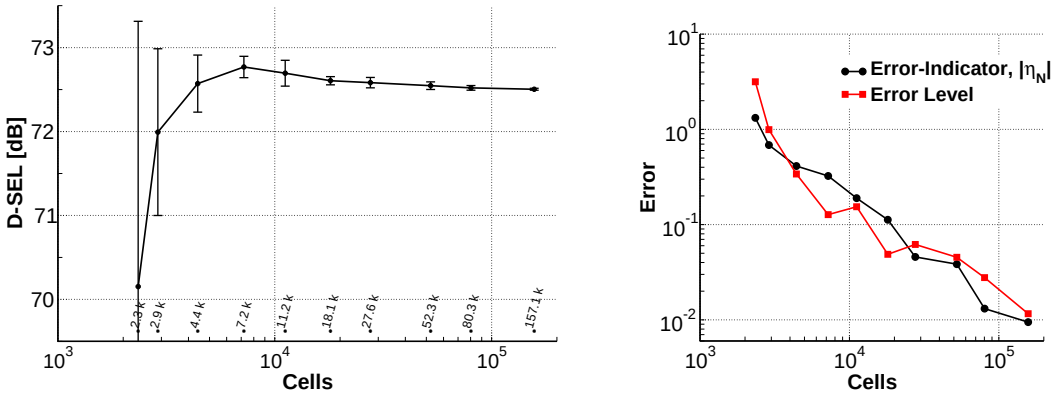
We use a uniform mesh-refinement study to verify if the output predictions are accurate. Figure 10 shows results from uniform refinement of the nearfield mesh over the first 7 cycles. The initial mesh is the same for both runs. We expect the adaptation to refine the highest-error cells, thereby obtaining a close approximation of the output on meshes with much fewer cells. Figure 10 shows that for both ground-signature and D-SEL values, the adaptation tracks the uniform refinement sequence to plotting accuracy. On the final meshes, the uniformly refined mesh contains almost three orders-of-magnitude more cells. While a more thorough error analysis is still required, it is clear that the adaptation in the nearfield domain is addressing the error levels in the farfield outputs.

Figure 11 shows the nearfield meshes after 9 adaptive refinements for both outputs to examine which regions receive the most refinement. The black line in each plot indicates the location of the line sensor, located half-a-chord below the airfoil. As expected, the highest refinement occurs in the region between the airfoil and the sensor, and especially in the near-body bow-shock region. Surprisingly, the domain of dependence of the farfield outputs in the nearfield domain is large. There is moderate refinement extending relatively far behind the airfoil and also in the cross-flow direction, as shown in the left-side plots of Fig. 11.

To explain this refinement pattern, we examine the farfield adjoint solution, Eq. 21. Figure 12 shows the adjoint solution (labeled Ψ, scaled) for both outputs plotted together with scaled nearfield and ground signatures in the retarded time coordinate τ. The range of τ in Fig. 12 corresponds to the length of the sensor in the nearfield domain (22 chords). Due to the large increase in the period of the signature, as already noted in Fig. 8, the adjoint values are non-zero over most of the sensor, especially for D-SEL. This forces the extent of the nearfield adjoint solution, Eq. 22, to reach many chords away from the airfoil, particularly into the wake region. Recall that the nearfield adjoints weight the nearfield residuals via Eq. 29 and Eq. 26. Upstream of the bow shock, there is no refinement because the nearfield residuals are zero. Downstream,

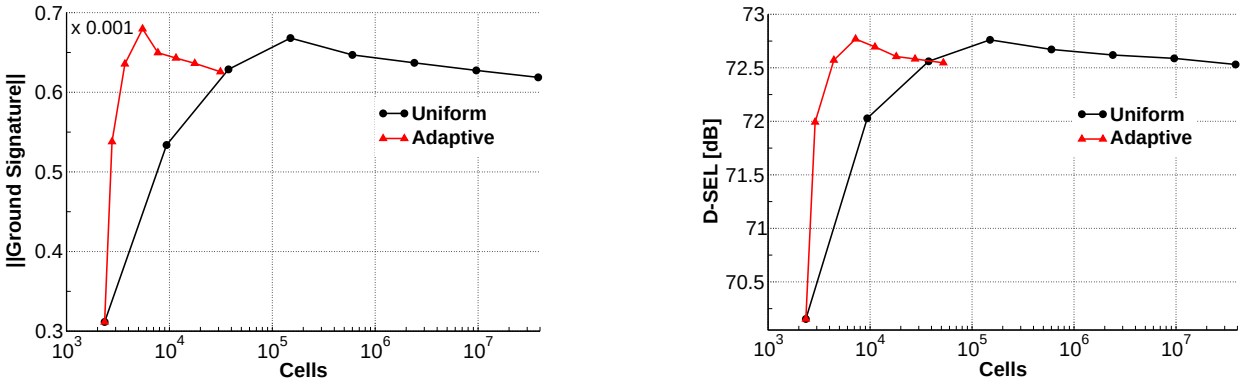


(a) Ground signature, Eq. 31



(b) D-SEL

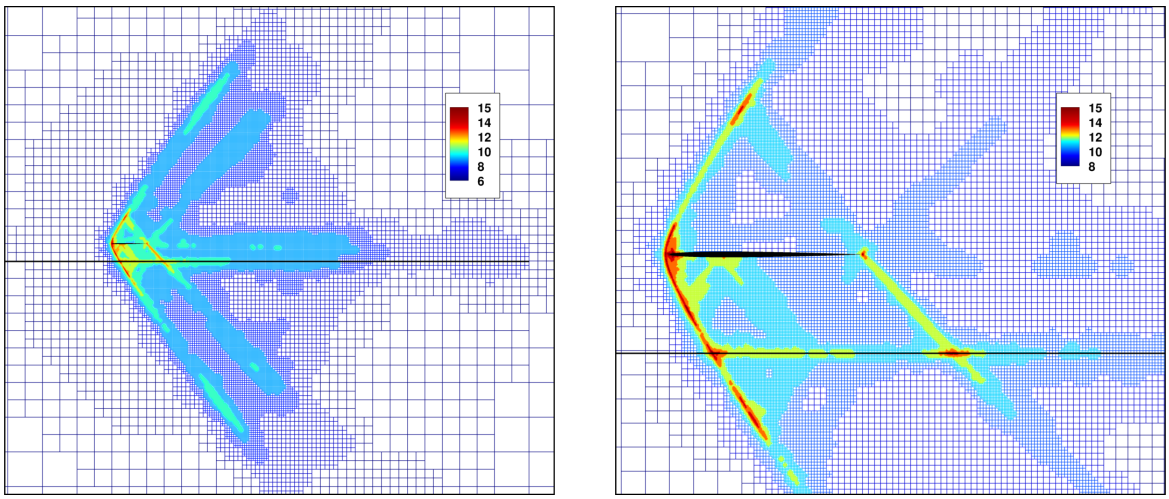
Figure 9: Convergence of farfield outputs as a function of adaptive refinement of the nearfield mesh. Error bars in plots on left indicate level of discretization error shown as red lines in plots on right.



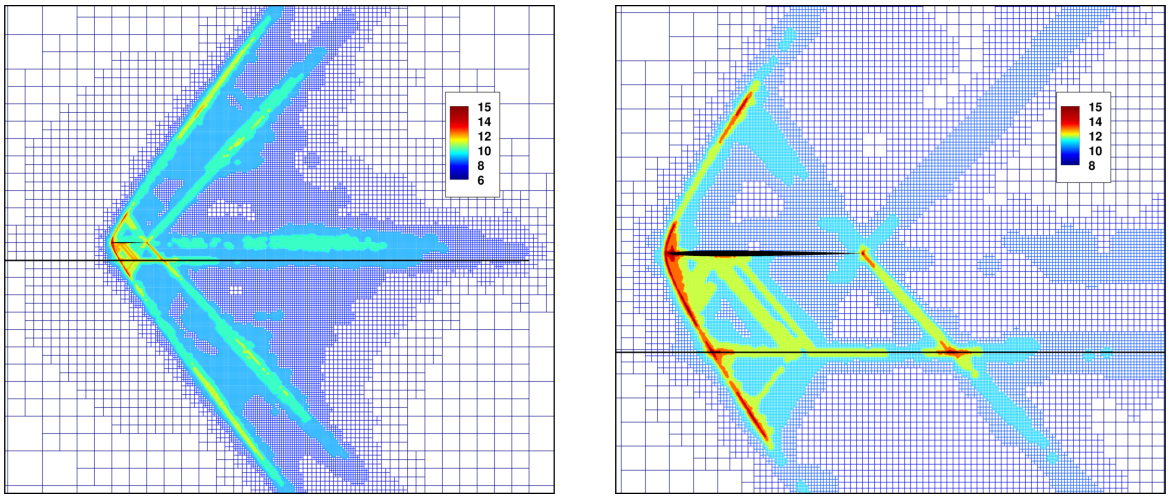
(a) Ground signature, Eq. 31

(b) D-SEL

Figure 10: Comparison of output accuracy between adaptive and uniform refinements of the nearfield domain for the NACA 0003 test case.



(a) Ground signature, Eq. 31



(b) D-SEL

Figure 11: NACA 0003 nearfield mesh after 9 adaptation cycles. Black line shows location of sensor to extract the signature. Close-up view of the airfoil region shown on right. Colors represent cell refinement levels, with dark reds showing the smallest cells.

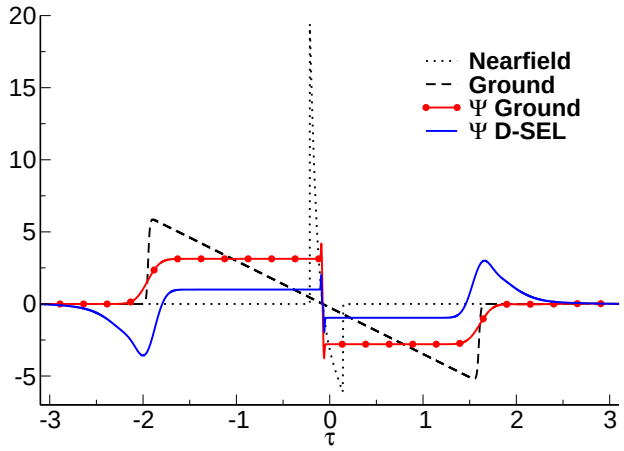


Figure 12: Farfield adjoint solutions, Ψ_F, for ground and D-SEL outputs plotted with nearfield and ground signatures.

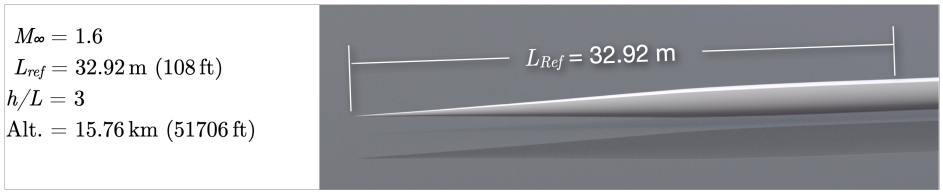


Figure 13: Geometry and conditions for the Axie test case

the nearfield residuals are non-zero, primarily due to the presence of shocks, resulting in the refinement patterns observed in Fig. 11. The large spread of the waveform that drives the domain of dependence in this problem is inadvertent, but it illustrates clearly the importance of the adjoint solution in the farfield. The spreading of the wave, however, is much larger than that observed for low-boom signatures. We examine more representative test cases for low-boom analysis next.

C. Multiple Target Outputs: Axie Geometry

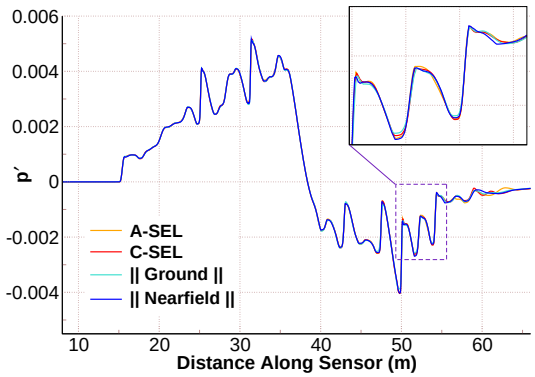
We now consider a benchmark problem in sonic-boom analysis. The model is the axisymmetric body of revolution (Axie) from the Second AIAA Sonic Boom Prediction Workshop (SBPW2).[5] Figure 13 shows a view of the geometry and summarizes the flow conditions. While the model appears smooth in the rendering, it is designed to produce a nearfield signature similar to that of the NASA Concept 25D model, also studied at SBPW2. The pressure signature is extracted from the nearfield domain three reference lengths below the body, $h/L = 3$. In this example we enable molecular relaxation in the farfield solver to obtain accurate ground signatures, but recall that the relaxation term is treated as a constant in the adjoint system, Eq. 21.

The goal of this example is to compare and contrast adaptation results with different target SEL metrics and the ground signature, and also with the established approach of adapting only on the nearfield signature. We use the nearfield output functional, colocated on line ℓ in Eq. 4, to extract the pressure signature $p' = (p - p_\infty)/p_\infty$ from Ω_N

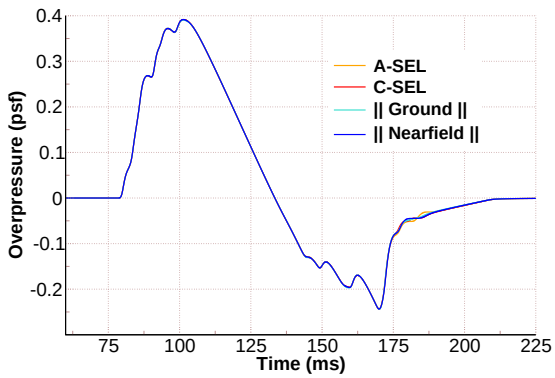
$$J_\text{N} = \int_0^L (p')^2 \, dl \tag{33}$$

and apply the single-discipline error analysis described in Sec. III-A. Studies of the Axie case using mesh adaptation for this output can be found in Ref. 20.

We perform four simulations using the target outputs J_N, J_G, J_A and J_C for the nearfield and ground signatures, and the A- and C-SEL metrics, respectively. In the nearfield, all simulations start from the same initial mesh, run for nine adaptation cycles and use the same mesh growth rate in each cycle. This means that the final number of cells in each simulation is roughly the same, which is useful when comparing adaptation patterns. In the farfield, all cases use 16,000 uniformly spaced points along the sensor. This corresponds to a sampling frequency of about 32 kHz that is chosen based on refinement study similar to that presented for the N-wave problem in Sec.V-A.



(a) Nearfield Signature



(b) Ground Signature

Figure 14: Signatures obtained with J_A (A-SEL), J_C (C-SEL), J_G (Ground) and J_N (Nearfield) outputs.

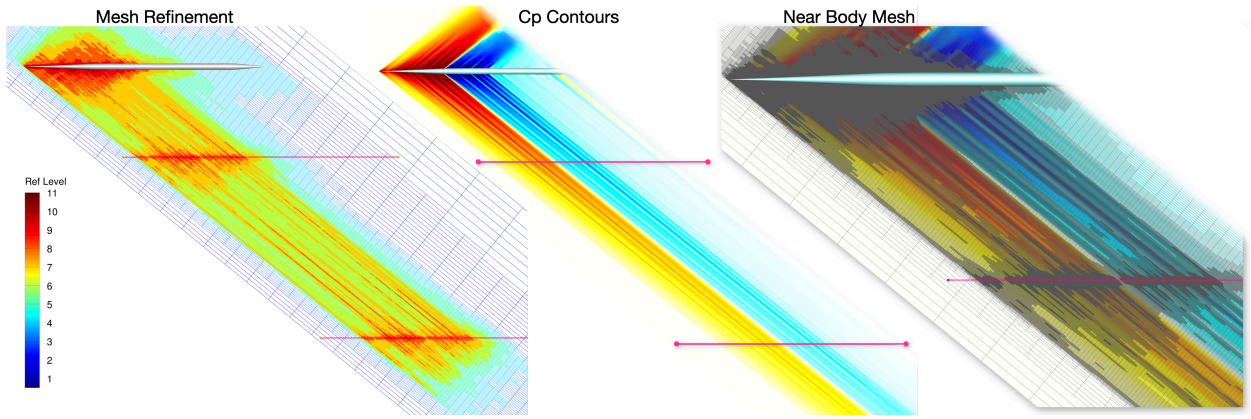


Figure 15: Final mesh containing 75.5 M cells and C_p distribution (red indicates high pressure and blue indicates low pressure) for the Axie body with adaptation driven by nearfield line sensors.

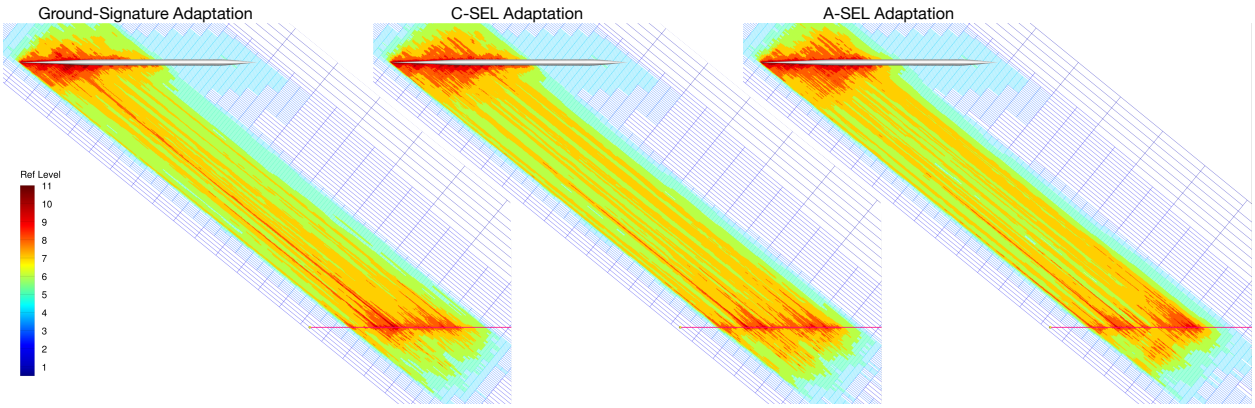


Figure 16: Final meshes colored by refinement level for simulations driven by farfield outputs: ground signature, C-SEL and A-SEL. Meshes have 76.2 M, 75.9 M, and 76.1 M cells, respectively.

Figure 14 shows the final signatures obtained from all simulations. Figure 14a displays a comparison of the nearfield signatures. Figure 14b shows the ground signatures. In both plots, the signatures are extremely similar and differ only slightly near the aft portion of the profiles. These comparisons show that all four simulations arrive at nearly identical signatures.

Figure 15 shows the final mesh and solution for adaptation driven by the nearfield output, J_N. This output is a combination of nearfield sensors at $h/L = 1$ and $h/L = 3$ based on an efficient setup presented at SBPW2.[20] The left frame shows the final mesh with cells colored by refinement level. The center frame shows the solution colored by contours of pressure coefficient, C_p. Observe the interaction of numerous shocks and expansions that form the nearfield signature shown in Fig. 14. The magenta lines show locations of the pressure sensors at $h/L = 1$ and $h/L = 3$. The right frame shows a close-up of the near-body region, extending from the geometry to just below the first pressure sensor.

Figure 16 shows final meshes for the three simulations using the farfield target outputs. The left frame shows the mesh obtained for the ground signature output J_G, the center frame for C-SEL and the right frame for A-SEL. It is interesting to contrast the adaptation patterns in the four meshes of Figs. 15 and 16 with the nearfield signature shown on the left side of Fig. 14. Overall, the ground signature output favors the peaks near the main expansion in the middle of the signature, while the nearfield signature and A-SEL outputs put more emphasis on the aft-portion of the waveform. Resolution for the C-SEL output is more balanced between the forward and aft peaks in the signature.

Figure 17 shows the adaptation convergence history for all four simulations. Similar to Fig. 9, the plots for the ground signature and loudness metrics show convergence of the farfield output with respect to the number of cells in the nearfield mesh. Two plots are shown for each simulation. The left frames show convergence of the target output (black line) with error bars representing the level of discretization error ε, Eq. 7. The right

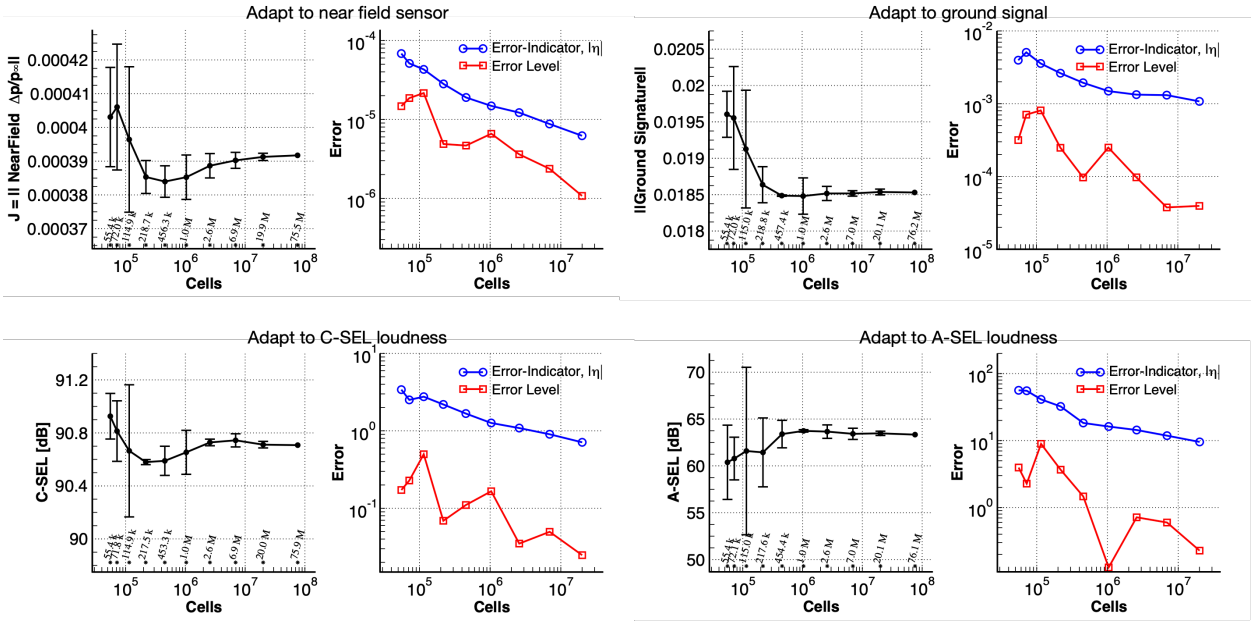


Figure 17: Convergence of target outputs and error estimates as a function of adaptive refinement of the nearfield mesh. Final meshes for these cases are shown in Figs. 15 and 16.

frames show convergence of both the error level ε (red lines) and the adaptation error indicator η_N (blue lines, Eq. 26). All four simulations converge well. The error levels generally decrease over the last three cycles and η_N is decreasing nearly linearly over the whole adaptation history. A-SEL converges to 63.3 ± 0.2 dB and C-SEL to 90.71 ± 0.02 dB, which is a notably low level of discretization error.

So far, the results demonstrate that when the goal of a simulation is a specific farfield output, the mesh adaptation procedure efficiently controls the error in that output. Interestingly, results in Fig. 14 show that simulations not directly targeting the ground signature predict the ground signature well. This motivates us to explore if this holds for other outputs. For example, when a mesh is adapted for the A-SEL output, are its C-SEL estimates credible? Put another way — what is the best target output to efficiently converge a specific set of loudness metrics?

Computed Ground Noise Metrics

Adaptation driven by	PL [dB]	A-SEL [dB]	B-SEL [dB]	C-SEL [dB]
A-SEL	77.686	63.335	77.068	90.668
C-SEL	77.783	63.338	77.162	90.708
|| Ground ||	77.828	63.430	77.182	90.702
|| Nearfield ||	77.732	63.332	77.141	90.708

Table 1: Comparison of all loudness metrics, including Perceived Loudness (PL), computed from simulations using the A-SEL, C-SEL, nearfield and ground signature adaptation targets.

We answer these questions in two steps. First, we evaluate all the loudness metrics for each of the four simulations on the finest mesh. Table 1 summarizes the results. The left column lists the target outputs of the four simulations. For each simulation, we list column-wise all the loudness metrics, including Perceived Loudness (PL). Agreement among the values is excellent. The maximum deviation is only 0.15 dB. C-SEL is particularly noteworthy with maximum spread of only 0.05 dB. Perceived loudness and B-SEL show the largest deviations at 0.142 and 0.114 dB, respectively. This is not unexpected since these were not the target functionals in any of the four simulations.

The second step requires the estimation of error levels in all the SEL values listed Table 1. We have a

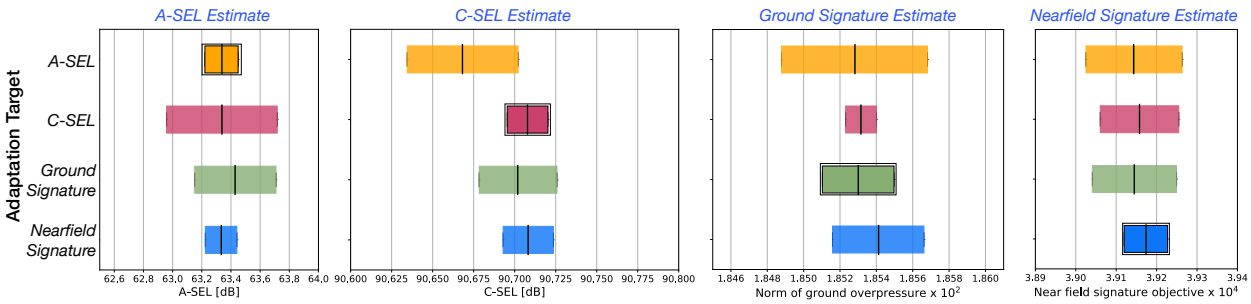


Figure 18: Error estimates for all outputs when the adaptation is driven by J_{A}, J_{C}, J_{G} and J_{N}. Outputs that match the adaptation functional are shown with thin black outlines.

hint from Fig. 17 that the values in Table 1 are within the level of discretization error for A- and C-SEL. To evaluate the error in the remaining values, in each of the four simulations we designate the non-target outputs as "passive" and use the error estimation procedure to monitor their error levels as the mesh evolves for the target functional. Figure 18 summarizes the results using simplified box-plots for each output. The four adaptation target outputs are listed on the left, and the individual frames show the value of each output on the final mesh. The widths of the shaded boxes correspond to the error levels for each output and the black vertical lines represent the values from Table 1. Narrower boxes correspond to tighter error estimates. Outputs that correspond to the adaptation target functional are highlighted with a thin black outline.

Figure 18 allows a quick comparison of the relative accuracy of each output. The figure shows that the error estimates are all reasonably tight – especially when the meshes are being tailored for a particular output. This follows intuition since we expect that the lowest errors are obtained for the target outputs. Figure 18 shows that even in this highly non-linear and multidisciplinary system, this is indeed the case. Nevertheless, there are some exceptions. For example, adaptation on C-SEL does a very good job of controlling error not only in C-SEL, but also in the ground signature – where it actually outperforms the simulation with J_{G} as the target output. However, it does not appear to be particularly good at controlling the error in A-SEL. Similarly, adaptation based on the nearfield sensors reaches low errors for not only the nearfield signature, but also in both A- and C-SEL. The behavior of the simulation with A-SEL as target output is also interesting. While it gives the tightest error estimates for A-SEL itself, it gives the poorest estimates for all the other metrics. Finally, note that the fact that all the boxes within any particular metric overlap supports the contention that all four simulations are close to the asymptotic range.

D. X-59 Loudness Analysis

For the final test, we examine a challenging analysis case featuring the X-59 flight demonstration aircraft to assess the benefits and robustness of the error estimation procedure on a practical engineering problem. Figure 19 shows the airframe, control surfaces, engine inlet and nozzle, and near-body flow solution. Observe that the shocks are much stronger along the upper surface of the aircraft, which is an important design feature to minimize sonic booms on the ground. The model includes three outflow boundaries to model inlets and five inflow boundaries to model exhaust nozzles. The aircraft geometry also includes vortex generators and various probes. The simulation is performed at $M_\infty = 1.4$, $\alpha = 2.09°$ and altitude of 53,200 ft.

We choose C-SEL as the target output and specify a line sensor three body lengths below the aircraft to transfer the signature from the nearfield domain to the farfield via Eq. 30. The propagation includes relaxation and is performed on a fine mesh $\mathcal{T}_{\mathrm{F,H}}$ of 50,000 nodes. Figure 20a shows convergence of C-SEL as a function of the number of cells in the nearfield domain. The initial mesh is coarse, containing only 75,000 cells. Once the mesh passes 10M cells, the discretization error (ε , Eqs. 7 and 29) systematically decreases and C-SEL levels out. After eight adaptations, the simulation reaches 152M cells and predicts a C-SEL value of 90.9 ± 0.3 dB. To understand the variations in C-SEL as the adaptation advances, Fig. 20b shows selected ground signatures corresponding to adaptation cycles marked in Fig. 20a. By the sixth adaptation, the positive phase, including the zero-crossing of the signature, is converged to plotting accuracy. The pressure recovery region, however, is still evolving, but the changes are diminishing. This is not surprising, since the aft region of the signature is affected by the aft portion of the X-59 geometry and the engine plume.

Figure 21 shows solution details in the nearfield domain to examine the morphology of the aft portion of

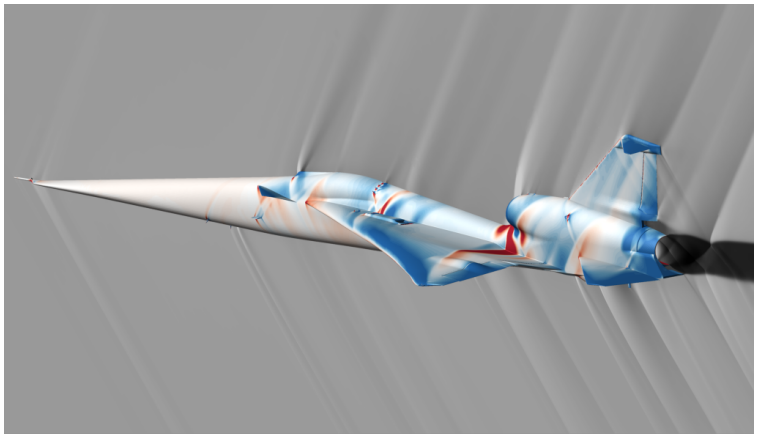
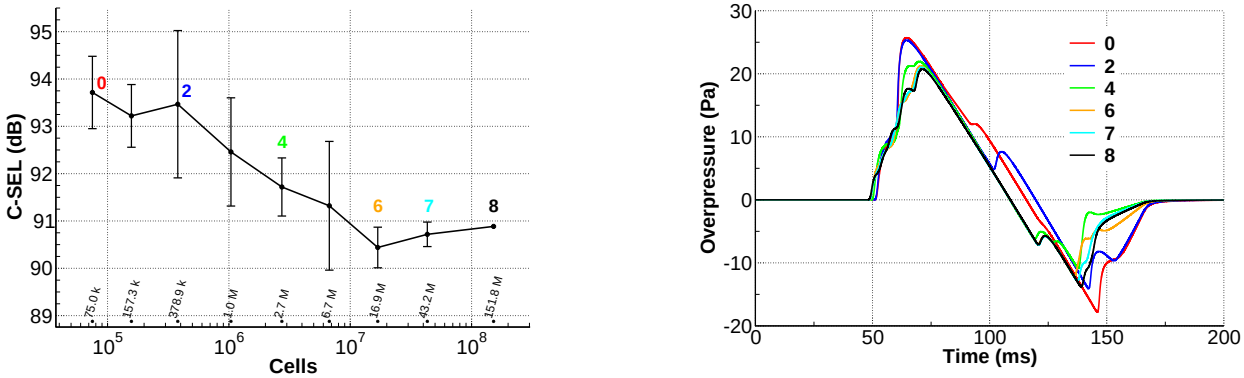


Figure 19: X-59 aircraft model and near-body flow ($M_\infty = 1.4$ and $\alpha = 2.09°$). Aircraft surface is colored by C_p (red denotes pressures above freestream, blue below). Gray scale is used to visualize the near-body shocks via density variations on a plane through the aircraft's centerline.



(a) C-SEL

(b) Ground Signature

Figure 20: Convergence of C-SEL and ground signature for the X-59 geometry

the nearfield signature and investigate plume effects. The figure shows a side-view of the finest nearfield mesh (center, colored by refinement levels), the evolution of the nearfield signature (lower left) and a close-up of the flow solution near the back of the aircraft (upper right). The initial mesh corresponds to refinement level 0 and we observe highest refinement levels near the aircraft, along the engine plume and the sensor, as well as the aft part of the signature. We use density contours to highlight the interaction of the tail shocks propagating through the plume (Fig. 21, upper right). This is the most challenging region of the nearfield because the plume boundaries and shock locations change with mesh refinement. It is these interactions that delay the convergence of the aft part of the ground signature, but the adaptation procedure handles these features robustly. Overall, this a promising result because it is remarkable to witness error control in the nearfield domain that improves the prediction of outputs located 22 km away based on two independent solvers in such a complex engineering problem. Furthermore, this approach could be well suited for boom-loudness database generation involving many operating conditions and aircraft configurations because simulation verification is straightforward when error analysis such as the one shown in Fig. 20a is readily available.

VI. Conclusions

The method of adjoint-weighted residuals has been applied to the nearfield-farfield domain decomposition approach that is frequently used to predict loudness of sonic booms. The approach provides an efficient way to estimate and control discretization error in one-way coupled, triangular systems when dealing with multiple independent solvers. We have modified the farfield solver to obtain an asymptotically consistent

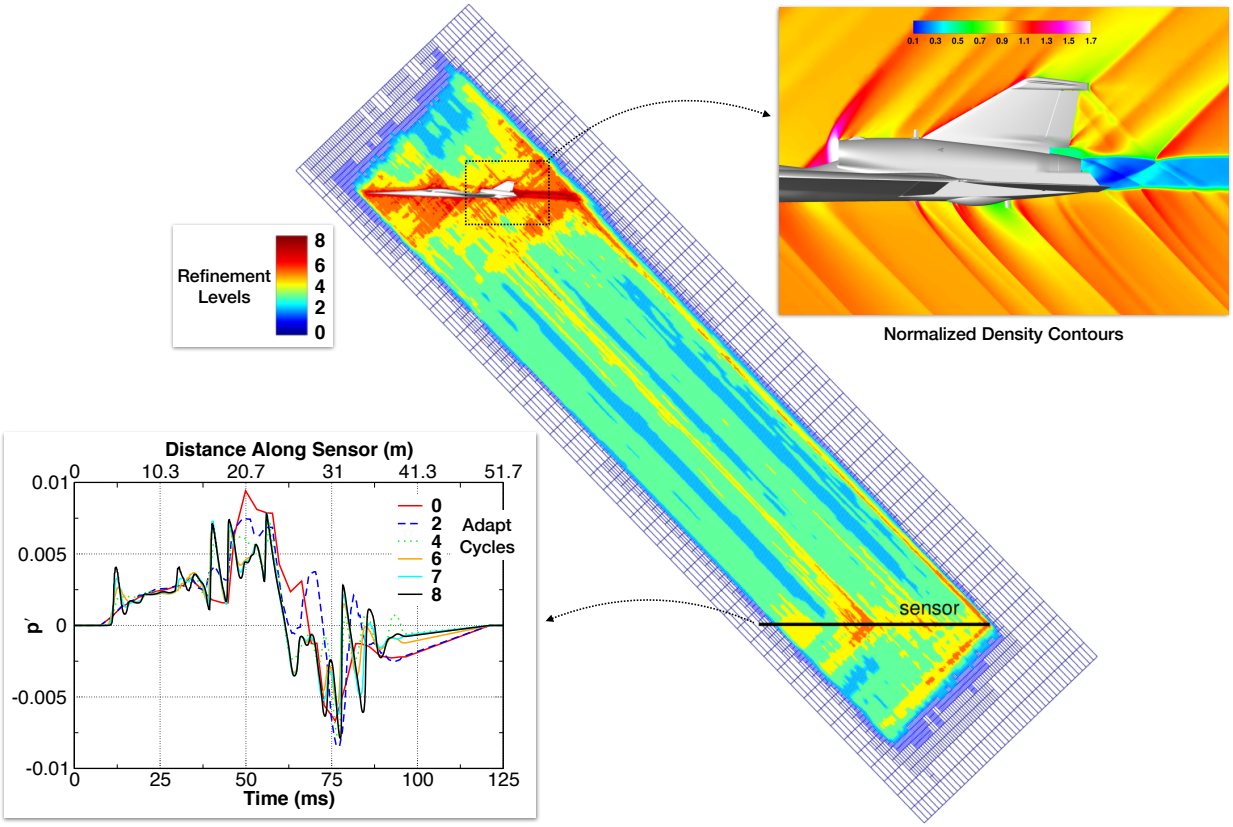


Figure 21: Nearfield details for the X-59 configuration. Lower-left frame shows evolution of the pressure signature driven by the C-SEL output. Middle frame shows the final mesh with cells colored by refinement level (dark reds represent smallest cells). Top-right is a close-up of the aft region of the aircraft, showing high resolution of the shock-plume interactions that propagate to the sensor.

adjoint discretization for all terms of the augmented Burgers' equation except molecular relaxation. Adjoint consistency is necessary for obtaining reliable error estimates and is demonstrated on the N-wave model problem. We show that the farfield outputs and gradients converge at a first-order rate, which is the expected order of accuracy. The test cases show that the approach correctly accounts for the influence of discretization errors in the nearfield domain on the farfield outputs. Moreover, the approach improves on the established practice of adapting only on the nearfield signature by providing credible error estimates on loudness predictions in an automatic fashion.

Near term plans include implementation of a higher-order discretization for the nonlinear term in the farfield solver. This could further reduce the number of points needed to discretize the signature and improve the efficiency of both primal and adjoint solves in the farfield. We also plan to complete the linearization of the relaxation process and investigate the influence of discretization errors from ray tracing. In addition, we plan to leverage the improved farfield adjoint solution for computing reliable gradients in aerodynamic shape optimization of low-boom aircraft.

Acknowledgements

The authors gratefully acknowledge support from the NASA ARMD Commercial Supersonic Technology Project. Resources supporting this work were provided by the NASA High-End Computing (HEC) Program through the NASA Advanced Supercomputing (NAS) Division at Ames Research Center. David Rodriguez was supported by NASA Ames Research Center contract NNA16BD60. The authors thank Prof. David Darmofal (MIT) for helpful discussions, and James Jensen (NASA Ames) and Wade Spurlock (STC) for reviewing the manuscript.

References

[1] "Low-Boom Flight Demonstration," https://www.nasa.gov/X59, Accessed: 2021-10-26.

[2] Maglieri, D. J., Bobbitt, P. J., Plotkin, K. J., Shepherd, K. P., Coen, P. G., and Richwine, D. M., "Sonic Boom: Six Decades of Research," NASA/SP-2014-622, 2014, http://hdl.handle.net/2060/20150006843.

[3] Page, J. A. and Plotkin, K. J., "An Efficient Method for Incorporating Computational Fluid Dynamics Into Sonic Boom Prediction," *9th AIAA Applied Aerodynamics Conference, Paper 91–3275*, Baltimore, MD, Sept. 1991.

[4] Meredith, K. B., Dahlin, J. H., Graham, D. H., Malone, M. B., Haering Jr., E. A., Page, J. A., and Plotkin, K. J., "Computational Fluid Dynamics Comparison and Flight Test Measurement of F-5E Off-Body Pressures," AIAA Paper 2005–0006, Jan. 2005.

[5] Park, M. A. and Nemec, M., "Nearfield Summary and Statistical Analysis of the Second AIAA Sonic Boom Prediction Workshop," *Journal of Aircraft*, Vol. 56, No. 3, 2019, pp. 851–875. doi:10.2514/1.C034866.

[6] Park, M. A. and Carter, M. B., "Low-Boom Demonstrator Near-Field Summary for the Third AIAA Sonic Boom Prediction Workshop," *Journal of Aircraft*, Vol. 0, Article in Advance, pp. 1–15. doi:10.2514/1.C036323.

[7] Rallabhandi, S. K. and Loubeau, A., "Summary of Propagation Cases of the Third AIAA Sonic Boom Prediction Workshop," *Journal of Aircraft*, Vol. 0, Article in Advance, pp. 1–17. doi:10.2514/1.C036327.

[8] Bradley, K. A., Hobbs, C. M., Wilmer, C. B., Sparrow, V. W., Stout, T. A., Morgenstern, J. M., Underwood, K. H., Maglieri, D. J., Cowart, R. A., Collmar, M. T., Shen, H., and Blanc-Benon, P., "Sonic Booms in Atmospheric Turbulence (SonicBAT): The Influence of Turbulence on Shaped Sonic Booms," NASA/CR 2020-220509, National Aeronautics and Space Administration, Center for AeroSpace Information, 7115 Standard Drive, Hanover, MD 21076, 2020, https://ntrs.nasa.gov/api/citations/20200002482/downloads/20200002482.pdf.

[9] Shen, H. and Lazzara, D., "A Space Marching Method for Sonic Boom Near Field Predictions," AIAA Paper 2016–2037, Jan. 2016. doi:10.2514/6.2016-2037.

[10] Housman, J. A., Kenway, G. K., Jensen, J. C., and Kiris, C. C., "Efficient Near-Field to Mid-Field Sonic Boom Propagation Using a High-Order Space Marching Method," AIAA Paper 2019–3487, June 2019. doi:10.2514/6.2019-3487.

[11] Yamashita, R., Wutschitz, L., and Nikiforakis, N., "A full-field simulation methodology for sonic boom modeling on adaptive Cartesian cut-cell meshes," *Journal of Computational Physics*, Vol. 408, 2020, pp. 1–19. doi:https://doi.org/10.1016/j.jcp.2020.109271.

[12] Yamashita, R., Makino, Y., and Roe, P. L., "Fast Full-Field Simulation of Sonic Boom Using Space Marching Method," AIAA Paper 2021–2618, June 2021. doi:10.2514/6.2021-2618.

[13] Cliff, S. E., Elmiligui, A. A., Campbell, R. L., and Thomas, S. D., "Refined Tetrahedral Meshes with Mach Cone Aligned Prisms for Sonic Boom Analysis," *Journal of Aircraft*, Vol. 50, No. 3, May 2013, pp. 778–790.

[14] Duensing, J. C., Jensen, J. C., Housman, J. A., Piotrowski, M. G., Maldonado, D., Sozer, E., Kiris, C. C., and Kenway, G. K., "Structured and Unstructured Simulations for the Third AIAA Sonic Boom Prediction Workshop," *Journal of Aircraft*, Vol. 0, Article in Advance, pp. 1–23. doi:10.2514/1.C036407.

[15] Vanharen, J., Loseille, A., Alauzet, F., and Park, M. A., "Nearfield Anisotropic Mesh Adaptivity for the Third AIAA Sonic Boom Workshop," AIAA Paper 2021–0347, Jan. 2021. doi:10.2514/6.2021-0347.

[16] Jones, W. T., Nielsen, E. J., and Park, M. A., "Validation of 3D Adjoint Based Error Estimation and Mesh Adaptation for Sonic Boom Prediction," AIAA Paper 2006–1150, Jan 2006.

[17] Wintzer, M., Nemec, M., and Aftosmis, M. J., "Adjoint-Based Adaptive Mesh Refinement for Sonic Boom Prediction," AIAA Paper 2008-6593, August 2008.

[18] Loseille, A., Dervieux, A., and Alauzet, F., "Fully anisotropic goal-oriented mesh adaptation for 3D steady Euler equations," *Journal of Computational Physics*, Vol. 229, 2010, pp. 2866–2897. doi:10.1016/j.jcp.2009.12.021.

[19] Nemec, M. and Aftosmis, M. J., "Toward Automatic Verification of Goal-Oriented Flow Simulations," NASA/TM 2014-218386, National Aeronautics and Space Administration, Center for AeroSpace Information, 7115 Standard Drive, Hanover, MD 21076, 2014, http://hdl.handle.net/2060/20150000864.

[20] Anderson, G. R., Aftosmis, M. J., and Nemec, M., "Cart3D Simulations for the Second AIAA Sonic Boom Prediction Workshop," *Journal of Aircraft*, Vol. 56, No. 3, 2019, pp. 896–911. doi:10.2514/1.C034842.

[21] Spurlock, W. M., Aftosmis, M. J., and Nemec, M., "Cartesian Mesh Simulations for the Third AIAA Sonic Boom Prediction Workshop," *Journal of Aircraft*, Vol. 0, Article in Advance, pp. 1–17. doi:10.2514/1.C036405.

[22] Becker, R. and Rannacher, R., "An optimal control approach to a posteriori error estimation in finite element methods," *Acta Numerica 2000*, 2001, pp. 1–102.

[23] Giles, M. B. and Pierce, N. A., "Adjoint error correction for integral outputs," *Error Estimation and Adaptive Discretization Methods in Computational Fluid Dynamics*, edited by T. Barth and H. Deconinck, Vol. 25 of *Lecture Notes in Computational Science and Engineering*, Springer-Verlag, 2002.

[24] Barth, T., "Numerical Methods and Error Estimation for Conservation Laws on Structured and Unstructured Meshes," Lecture notes, von Karman Institute for Fluid Dynamics, Series: 2003-04, Brussels, Belgium, March 2003.

[25] Venditti, D. A. and Darmofal, D. L., "Grid Adaptation for Functional Outputs: Application to Two-Dimensional Inviscid Flow," *Journal of Computational Physics*, Vol. 176, 2002, pp. 40–69. doi:10.1006/jcph.2001.6967.

[26] Fidkowski, K. J. and Darmofal, D. L., "Review of Output-Based Error Estimation and Mesh Adaptation in Computational Fluid Dynamics," *AIAA Journal*, Vol. 49, No. 4, April 2011, pp. 673–694. doi:10.2514/1.J050073.

[27] Rallabhandi, S. K. and Park, M. A., "Adjoint-Based Mesh Adaptation for the Sonic Boom Signature Loudness," AIAA Paper 2017–3049, June 2017. doi:10.2514/6.2017-3049.

[28] Estep, D., Tavener, S., and Wildey, T., "A posteriori error estimation and adaptive mesh refinement for a multiscale operator decomposition approach to fluid–solid heat transfer," *Journal of Computational Physics*, Vol. 229, No. 11, 2010, pp. 4143–4158. doi:https://doi.org/10.1016/j.jcp.2010.02.003.

[29]Richter, T., "Goal-oriented error estimation for fluid-structure interaction problems," *Computer Methods in Applied Mechanics and Engineering*, Vol. 223–224, 2012, pp. 28–42. doi:10.1016/j.cma.2012.02.014.

[30]Copeland, S. R., Lonkar, A. K., Palacios, F., and Alonso, J. J., "Adjoint-Based Goal-Oriented Mesh Adaptation for Nonequilibrium Hypersonic Flows," AIAA Paper 2013–0552, Grapevine, TX, Jan. 2013.

[31]Carey, V., Estep, D., and Tavener, S., "A Posteriori Analysis and Adaptive Error Control for Multiscale Operator Decomposition Solution of Elliptic Systems I: Triangular Systems," *SIAM Journal on Numerical Analysis*, Vol. 47, No. 1, 2009, pp. 740–761. doi:10.1137/070689917.

[32]Rallabhandi, S. K., "Advanced Sonic Boom Prediction Using the Augmented Burgers Equation," *J. Aircraft*, Vol. 48, No. 4, 2011, pp. 1245–1253. doi:10.2514/1.C031248.

[33]Rallabhandi, S. K., Nielsen, E. J., and Diskin, B., "Sonic-Boom Mitigation Through Aircraft Design and Adjoint Methodology," *Journal of Aircraft*, Vol. 51, No. 2, 2014, pp. 502–510. doi:10.2514/1.C032189.

[34]Cleveland, R. O., *Propagation of Sonic Booms Through a Real, Stratified Atmosphere*, Ph.D. thesis, The University of Texas at Austin, 1995.

[35]Yamamoto, M., Hashimoto, A., Aoyama, T., and Sakai, T., "A unified approach to an augmented Burgers equation for the propagation of sonic booms," *J. Acoust. Soc. Am.*, Vol. 137, No. 4, 2015, pp. 1857–1866. doi:10.1121/1.4916833.

[36]Roache, P. J., "Verification of Codes and Calculations," *AIAA Journal*, Vol. 36, No. 5, May 1998, pp. 696–702.

[37]van Leer, B., "Flux-Vector Splitting for the Euler Equations," ICASE Report 82-30, Sept. 1982.

[38]Aftosmis, M. J., Berger, M. J., and Adomavicius, G., "A Parallel Multilevel Method for Adaptively Refined Cartesian Grids with Embedded Boundaries," AIAA Paper 2000–0808, Reno, NV, Jan. 2000.

[39]Aftosmis, M. J., Berger, M. J., and Murman, S. M., "Applications of Space-Filling-Curves to Cartesian Methods for CFD," AIAA Paper 2004–1232, Reno, NV, Jan. 2004.

[40]Berger, M. J., Aftosmis, M. J., and Murman, S. M., "Analysis of Slope Limiters on Irregular Grids," AIAA Paper 2005–0490, Reno, NV, Jan. 2005.

[41]Rodriguez, D. L., Aftosmis, M. J., and Nemec, M., "Formulation and Implementation of Inflow/Outflow Boundary Conditions to Simulate Propulsive Effects," AIAA Paper 2018-0334, Kissimmee, FL, Jan. 2018. doi:10.2514/6.2018-0334, AIAA SciTech Forum.

[42]Nemec, M., Rodriguez, D. L., and Aftosmis, M. J., "Adjoint-Based Mesh Adaptation and Shape Optimization for Simulations with Propulsion," AIAA Paper 2019-3488, June 2019. doi:10.2514/6.2019-3488.

[43]"Automated Triangle Geometry Processing for Surface Modeling and Cartesian Grid Generation (Cart3D)," https://software.nasa.gov/software/ARC-14275-1, Accessed: 2022-04-29.

[44]"sBOOM2: An Advanced Sonic Boom Propagation and Design Tool," https://software.nasa.gov/software/LAR-18477-1, Accessed: 2022-04-29.

[45]"3rd AIAA Sonic Boom Prediction Workshop," https://lbpw.larc.nasa.gov/sbpw3, Accessed: 2022-05-01.

[46]Alauzet, F. and Pironneau, O., "Continuous and discrete adjoints to the Euler equations for fluids," *International Journal for Numerical Methods in Fluids*, Vol. 70, No. 2, 2012, pp. 135–157. doi:https://doi.org/10.1002/fld.2681.

[47]Jayasinghe, S., Darmofal, D. L., Galbraith, M. C., Burgess, N. K., and Allmaras, S. R., "Adjoint analysis of Buckley-Leverett and two-phase flow equations," *Computational Geosciences*, Vol. 22, 2018, pp. 527–542.